Terahertz quantum cascade laser based optical coherence tomography

Citation: Lee, Alan W. M., Tsung-Yu Kao, Qing Hu, and John L. Reno " Terahertz quantum cascade laser based optical coherence tomography ", Proc. SPIE 8585, Terahertz and Ultrashort Electromagnetic Pulses for Biomedical Applications, 858508 (February 23, 2013). ©2013 SPIE.

As Published: http://dx.doi.org/10.1117/12.2001127

Publisher: SPIE

Persistent URL: http://hdl.handle.net/1721.1/87068

Version: Final published version: final published article, as it appeared in a journal, conference proceedings, or other formally published context

Terahertz quantum cascade laser based optical coherence tomography

Alan Wei Min Lee[a,b,*], Tsung-Yu Kao[b], Qing Hu[b], and John L. Reno[c]
[a] LongWave Photonics LLC, Boston, MA USA
[b] Massachusetts Institute of Technology, Cambridge, MA USA
[c] Sandia National Laboratories, Albuquerque, NM USA
*Corresponding author: awmlee@longwavephotonics

ABSTRACT

The interfaces of a dielectric sample are resolved in reflection geometry using light from a frequency agile array of terahertz quantum-cascade lasers. The terahertz source is a 10-element linear array of third-order distributed feedback QCLs emitting at discrete frequencies from 2.08 to 2.4 THz. Emission from the array is collimated and sent through a Michelson interferometer, with the sample placed in one of the arms. Interference signals collected at each frequency are used to reconstruct an interferogram and detect the interfaces in the sample. Due to the long coherence length of the source, the interferometer arms need not be adjusted to the zero-path delay. A depth resolution of 360 μm in the dielectric is achieved with further potential improvement through improved frequency coverage of the array. The entire experiment footprint is <1 m × 1 m with the source operated in a compact, closed-cycle cryocooler.

Keywords: terahertz, quantum cascade laser, tomography

1. INTRODUCTION

Tomography of dielectric thin films using terahertz frequency radiation (300 GHz to 10 THz) has found recent practical applications for the characterization of industrial polymers [1]. The non-ionizing nature of THz radiation and its strong response to water content also makes it suitable for characterization of biomaterials such as corneas [3] and teeth.

Comparing to the current commercial terahertz systems using nonlinear generation mechanisms, quantum-cascade lasers (QCLs) are a promising fundamental source of terahertz frequency radiation for their multi milliwatt power levels, electrical operation, and absence of optical alignment. However, the use of QCLs for the tomography of dielectric films is challenging due to the lack of picosecond pulsed sources necessary for time-of-flight tomography or the practical frequency tuning mechanisms necessary for interferometry based tomography. In this paper we report a frequency agile QCL source and the demonstration of tomography using the swept-source optical coherence tomography technique [6]. The letter is divided into sections detailing different key components of the THz swept-source optical coherence tomography system (SS-OCT) system. Section 2 details the working principles of SS-OCT. Section 3 reports the design of third-order distributed feedback THz quantum cascade lasers and detailed characterization of such a laser array. Section 4 describes the measurement result of the OCT system on dielectric thin film and the algorithm for retrieving the depth and interface information. Section 5 will discuss the recent improvement on 3rd DFB design to further improve the frequency coverage.

2. SWEPT-SOURCE OPTICAL COHERENCE TOMOGRAPHY (SS-OCT)

The frequency tunable source of the SS-OCT system is used to generate a tomographic profile (see Figure 1) of a sample, whose resolution is dependent on the bandwidth of the source. This profile is obtained by processing the interferometric signal, S, for each wavelength, λ_i, incident on the detector:

$$S_i[\Delta x] = \rho \sum_{j=1}^{M} \left[P_{R,i} + P_{S,i,j} + 2\sqrt{P_{R,i} P_{S,i,j}} \cdot cos\left(\frac{4 \cdot \pi}{\lambda_i} \cdot (\Delta x + x_j) \right) \right] \quad (1)$$

Terahertz and Ultrashort Electromagnetic Pulses for Biomedical Applications, edited by Gerald J. Wilmink, Bennett L. Ibey,
Proc. of SPIE Vol. 8585, 858508 · © 2013 SPIE · CCC code: 1605-7422/13/$18 · doi: 10.1117/12.2001127

Here ρ is the responsivity of the detector, $P_{R,i}$ is the measured power from the reference arm, $P_{S,i,j}$ is the measured power from the j^{th} interface in the sample, Δx is the path length difference between the sample and the reference arms, and x_j is the thickness of the j^{th} layer. Taking a summation over i (i.e. adding the signal from all the discrete wavelengths in the tunable source), results in the waveforms shown in Figure 1. The first column is for a single interface (j = 1) at Δx = 0 i.e. only a mirror in the sample arm. The second column shows the result for a sample with two interfaces (j = 2), whose thickness is x_j = - 1 mm. Here the sinusoids tend to cancel except when $\Delta x = x_1 = 0$ and when $\Delta x = x_2 = -1$ mm. As a result, an interface at -1 mm is clearly visible, where the strength of the signal is related to the discontinuity of the interface. In (1), weaker terms occurring from reflections within the sample are ignored.

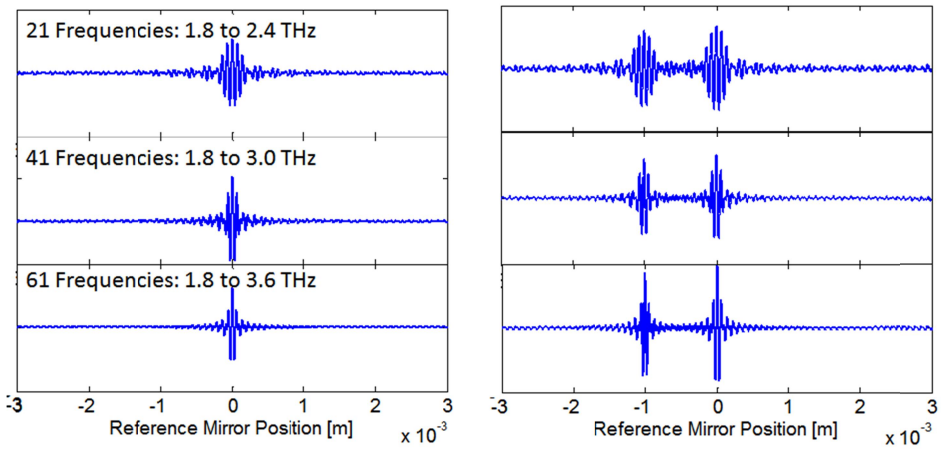

Figure 1. Figure of simulated interference signal resulting from SS-OCT scan. Left column shows the signal from a single interface (a mirror) placed in the sample arm. Right column shows the signal from a dielectric sample. Increasing the bandwidth of the source results in better resolution.

The axial resolution of the interface is proportional to how quickly the sinusoids cancel with respect to Δx, which is proportional to the bandwidth of the source:

$$\delta = \frac{c}{2n\Delta f} \tag{2}$$

Here δ is the depth resolution, c is the speed of light, n is the optical index of the material and Δf is the bandwidth of the tunable source. The increased resolution is apparent when looking at the rows of Figure 1 which have increasing amounts of bandwidth. For example, for a system with 21 frequencies spanning 1.8 THz to 2.4 THz, a resolution of 125 μm would result (n=1). This expression only represents the full width at half maximum (FWHM) of a detected interface (e.g. the FWHM of the envelope of Figure 1). If the SNR of the returned signal is high, smaller interface separations can be sub-resolved. Therefore the depth resolution is dependent on the frequency bandwidth of the QCL source, and to a lesser degree, its output power.

3. TERAHERTZ RADIATION SOURCE: THE QUANTUM CASCADE LASER

3.1 Key Component: 3rd order DFB QCL

To control the emission frequency of a QCL, a distributed feedback (DFB) grating fabricated into metal-metal waveguide can be used [8]. First-order gratings, where the grating periodicity, Λ, is half a guided wavelength ($\Lambda \approx \lambda/2$) have been demonstrated in single mode operation. However, the subwavelength dimensions of the optical waveguide result in highly divergent beam patterns exceeding 180°. A unique solution to control the beam divergence has recently been demonstrated using third-order gratings ($\Lambda \approx 3 \cdot \lambda/2$) [9]. This 3rd order DFB takes advantage of grating spacing, and the optical index (n~3.5-3.6 at 2-5 THz) of the GaAs/GaAlAs multiple quantum wells (MQW) gain medium, effectively making the laser an end-fire linear antenna array – and therefore a narrow emitter. The small footprint of this type of laser makes it ideal for dense array implementation. A series of 3rd order DFB QCLs of linear frequency

differences can be fabricated next to each other with a distance of 150 μm or less. Using current THz QCL fabrication techniques we can pack up to 21 QCLs on a single die.

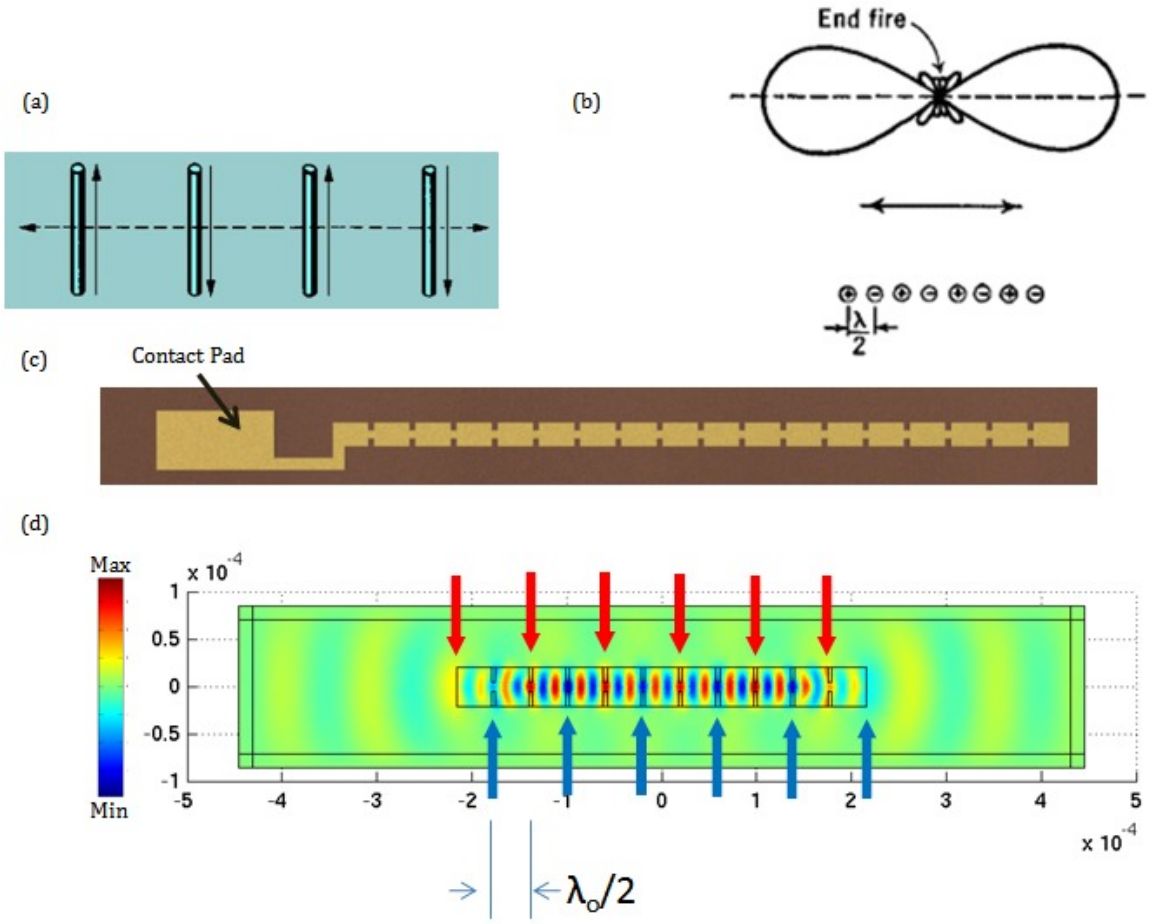

Figure 2. Part (a), schematic of a linear end-fire antenna array. Each rod (antenna) has 180 degree phase shift and is $\lambda_o/2$ from its neighbor, resulting in constructive interference in the array direction. Part (b), the calculated beam pattern of an end-fire antenna array. Part (c), the top schematic view of a corrugated 3rd order DFB QCL. Part (d), the electric field of the designed mode inside a 3rd order DFB laser. The arrows indicate the aperture from which field is radiated. Adjacent apertures alternate signs indicating a π phase shift. Because the apertures are close to $\lambda_o/2$ apart, endfire emission results.

To understand how the 3rd order grating operates, one can adopt the concept of a linear phased array (Figure 2 (a)). Here a series of antennas are spaced by $\lambda_0/2$, where λ_0 is the free space wavelength, and adjacent antennas are phase-shifted by π (indicated by arrows). Constructive interference from different antennas will form a narrow beam in the direction along the array. Part (c) shows a 3rd order DFB grating fabricated in a metal-metal waveguide, where the "antennas" from the phased array example are narrow sections or apertures. The electric field inside each aperture (part d) will be at its peak value with the phase adjacent apertures differing by π. Since the optical index of the gain medium is close to 3, the apertures are very close to $\lambda_o/2$ apart. Constructive interference results and forms a narrow beam pattern in the direction along the laser ridge. The divergence of the beam pattern is inversely-scaled with the square root of the number of the grating apertures (or the total length of the laser).

To obtain accurate frequency calculations and detailed grating parameter designs for third-order grating DFB lasers, full-wave three-dimension finite element method (FEM) simulations are required. An FEM simulation can determine all the modes supported in the laser structure along with the optical losses due to radiation, which we loosely term "gain threshold" [10]. Gain thresholds are plotted versus frequency for all resonant modes to obtain the plot shown in Figure 3.

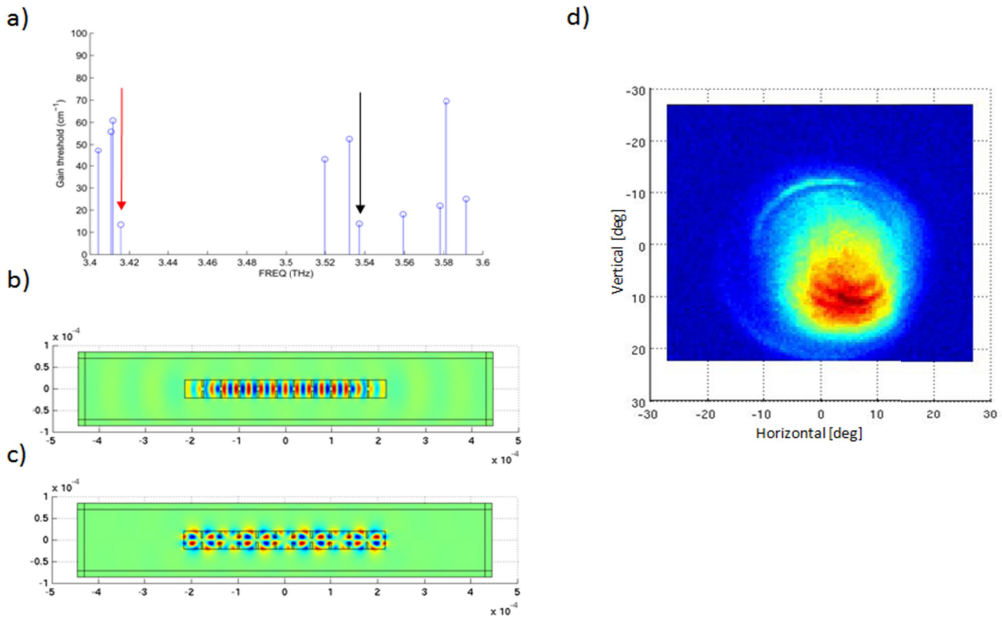

Figure 3. Part (a), a typical plot of the gain threshold of 3rd order DFB QCLs (corrugated structures). The designed mode (red arrow) has the lowest threshold and is thus most likely to lase, with other modes (black arrow) with similar losses competing for gain. Part (b), the simulated magnetic field corresponding to the designed mode (red arrow part a). The mode is clearly the fundamental lateral mode and also shows strong 3rd order grating effect ($\Lambda \sim 3\lambda/2$, where λ is guided wavelength). Part (c), the simulated magnetic field in the second lowest threshold mode (black arrow, part a). This mode is a hybrid mode consisting of several high-order lateral modes. Part (d) shows a measured far-field beam-pattern of a 3rd order DFB QCL.

3.2 Results of Frequency Agile 3rd order DFB QCL Array

The resulted QCL arrays after two iterations are shown in Figure 4. From the right of the figure, each device is numbered 1 through 21. The array is designed so that if all the devices are lasing in the correct mode, and the gain bandwidth of the QCL array is broad enough, frequency coverage will be from 1.8 THz (device 1) up to 2.6 THz (device 21). The devices were fabricated using standard metal-metal waveguide fabrication techniques [11], using contact lithography and Electron Cyclotron Resonance-Reactive Ion Etch (ECR-RIE) to define the laser mesas. Here the metallization on top of the device serves as a mask, resulting nearly vertical sidewalls, preventing lateral current spreading and bias non-uniformity. The device was indium soldered to a copper substrate for mounting in the cryocooler. Electrical contact was made by wirebonds between the QCL bonding pads, and an external printed circuit board with a pluggable header for easy removal of the module.

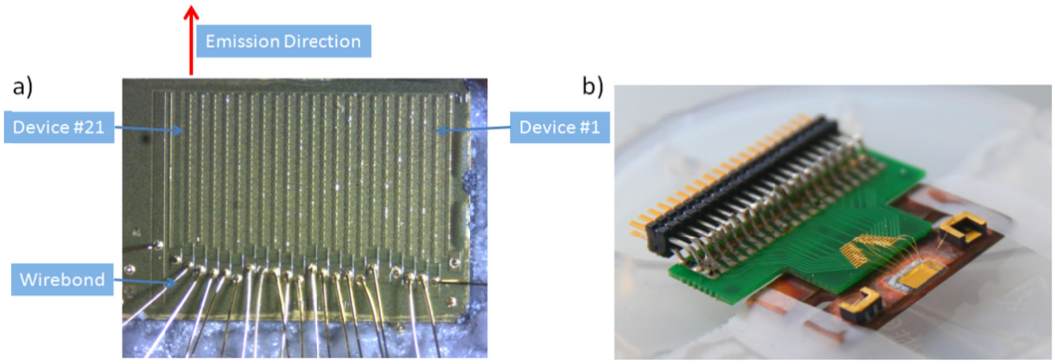

Figure 4. Part (a), image of a 3rd order DFB QCL array (corrugated structure) which emits in endfire mode. Electrical biasing is through a bonding pad shown with attached wirebonds. Part (b), shows the packaged QCL array. The array is indium soldered to a copper substrate, and wirebonds are made to the PCB. A standard connection header (0.05" pitch) is used for reliability and replaceability.

Individual QCLs were lost during the wire bonding process, due to the relatively small (150-μm pitch) bonding pads. The surviving devices were tested in pulsed mode (500 ns at ~10% duty cycle) at 48 K with the resulting spectra measured by Fourier transform infrared spectroscopy (FTIR) shown in Figure 5. Thresholds current densities range from 290 A/cm^2 to 340 A/cm^2 across whole array. From Device 9, a continuous increase in lasing frequency was observed for each device up to Device 19, spanning a frequency range of 2.08 to 2.4 THz. Device 7 and 8 lased around 2.3 and 2.5 THz. This type of mode hopping behavior is attributed to the relative position between the designed DFB modes and the peak gain frequency of the gain medium (see dashed-line in Figure 5). The maximum achievable frequency range is limited by the gain bandwidth of the QCL, the mode selectivity (difference in loss) of the optical modes, and the spacing between the modes. Peak optical power for individual laser was measured using a thermo-pile power meter (Scientech AC2500H) with peak power ~1.5 mW for device 16, whose lasing frequency is at the peak gain frequency of the gain medium. Device 9 has only ~ 150 μW peak power since it lased far from the peak gain frequency.

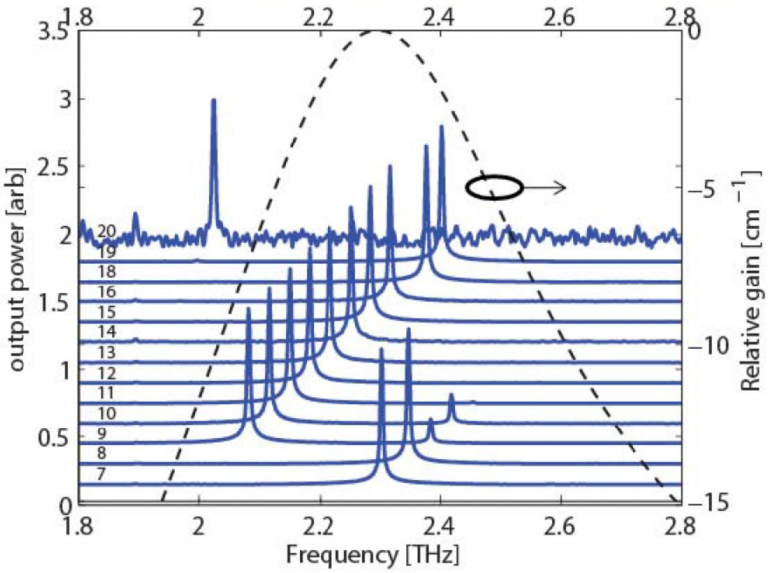

Figure 5. Spectra of DFB QCL array showing frequency separation ~30GHz. Devices 9 through 19 show frequency coverage of 320GHz. Dashed line indicates measured gain bandwidth of the QCL active region which peaks ~2.3 THz.

4. THZ SS-OCT SYSTEM RESULTS

The prototype OCT system is shown in Figure 6 and consists of: QCL residing in a closed cycle, cryogen free, Stirling Cycle cryocooler; an f/1 silicon lens to collimate the beam emerging from the cooler; a quartz beam splitter; a movable reference mirror; an f/1 silicon lens to focus the reflected light; a Ga:Ge photodetector. The compact Stirling cycle cryocooler is powered by 120 V and is controlled through a USB interface to actively maintain a cold finger temperature of 48 K (with 120 W electrical power consumption). The cryocooler system is compact (footprint 32 cm × 38 cm), relatively light (12 kg), and rated for MTTF of 25,000 hours, which will ultimately lead to a system that can be demonstrated in the field. The cryocooler is capable of cooling the device to 35 K, or dissipating 9 W of electrical power at 77 K – a temperature at which the devices are anticipated to operate efficiently. The 9 W power dissipation should be sufficient for continuous wave operation. A custom vacuum shroud including vacuum electrical feed-through for a 40 pin connector, and optical access were fabricated.

Custom bias electronics were fabricated and allow the software to select up to 16 different devices (limited by the MUX IC used in the hardware). The laser biasing electronics for the laser array, depicted schematically in Figure 7, consist of two boards: a PC interface/timing control board enabled by FPGA, and a power supply/modulation board which powers a device via a 1x16 multiplexing circuit. The FPGA board consists of a USB interface for interfacing the PC with the onboard microcontroller and an Altera FPGA. This microcontroller/FPGA combination was selected for maximum

flexibility in implementing the timing signals. These timing signals are used to synchronously bias the laser, and trigger the boxcar integrator/ADC/lock-in amplifier for detection. This board also generates laser select signals and the variable power supply control signals for the MUX/BIAS board, combing with Matlab GUI based software, the system allows <10 ms cycling though 16 QCL devices, and therefore rapid frequency switching.

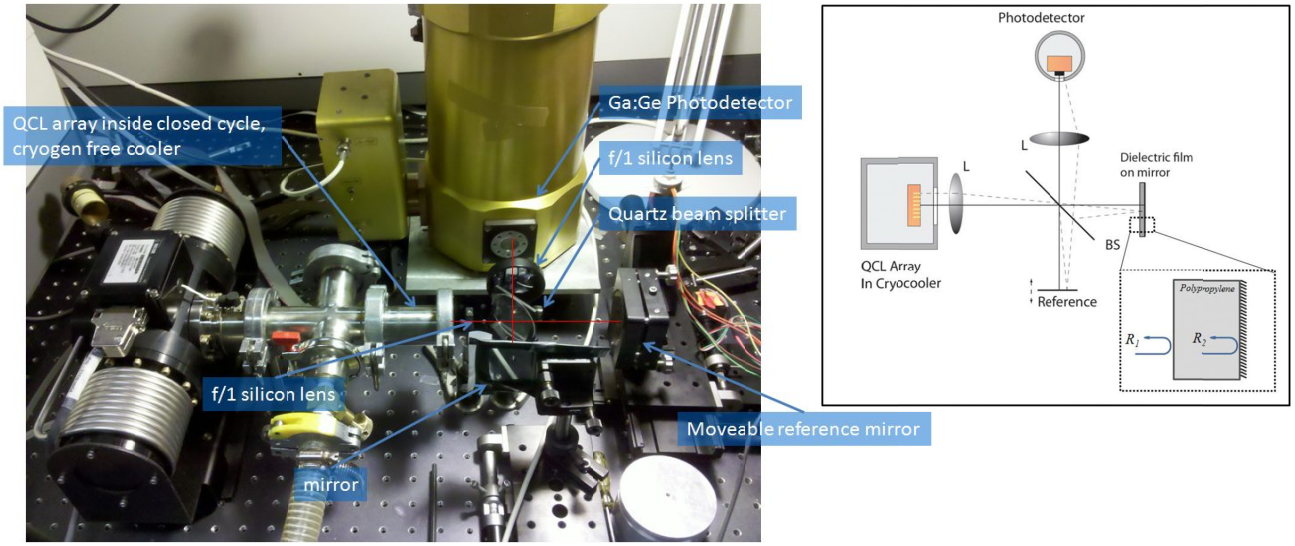

Figure 6. Prototype OCT system includes: a multi-element frequency agile QCL array residing in a compact Stirling cycle cryocooler (cryogen free); an interferometer; a Ge:Ga terahertz photodetector. Beam path through the interferometer shown in red. (on the right) the schematic for the similar optical setup is also shown.

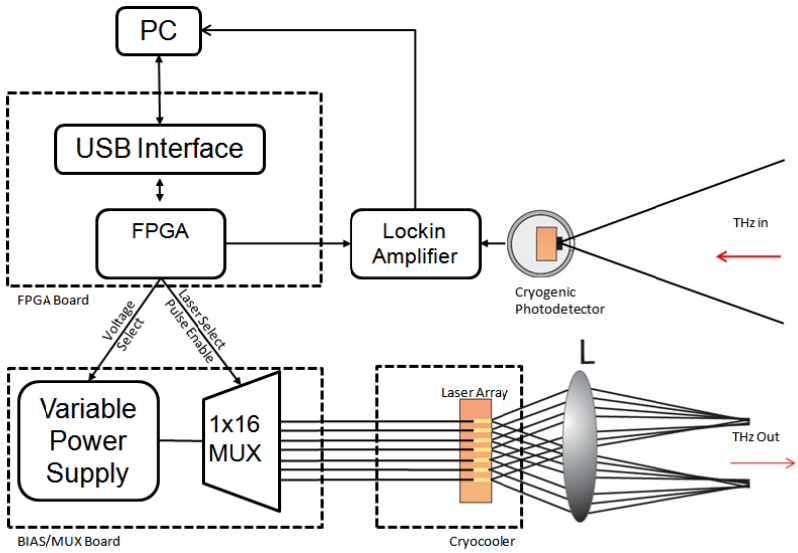

Figure 7. Overview of electronics for the SS-OCT experiment.

Interferometry measurements were taken in pulsed mode (500 ns pulse width 7% duty cycle), with either a mirror in the sample arm (for normalization) or a 380-µm thick piece of polypropylene in front of the sample mirror. In either case, the reference was stepped 30 times over a total distance of 140 µm. At each step, the signal was acquired via lock-in amplifier at the pulse repetition rate, for each of the lasers, resulting in the interferometric signals shown in Figure 8.

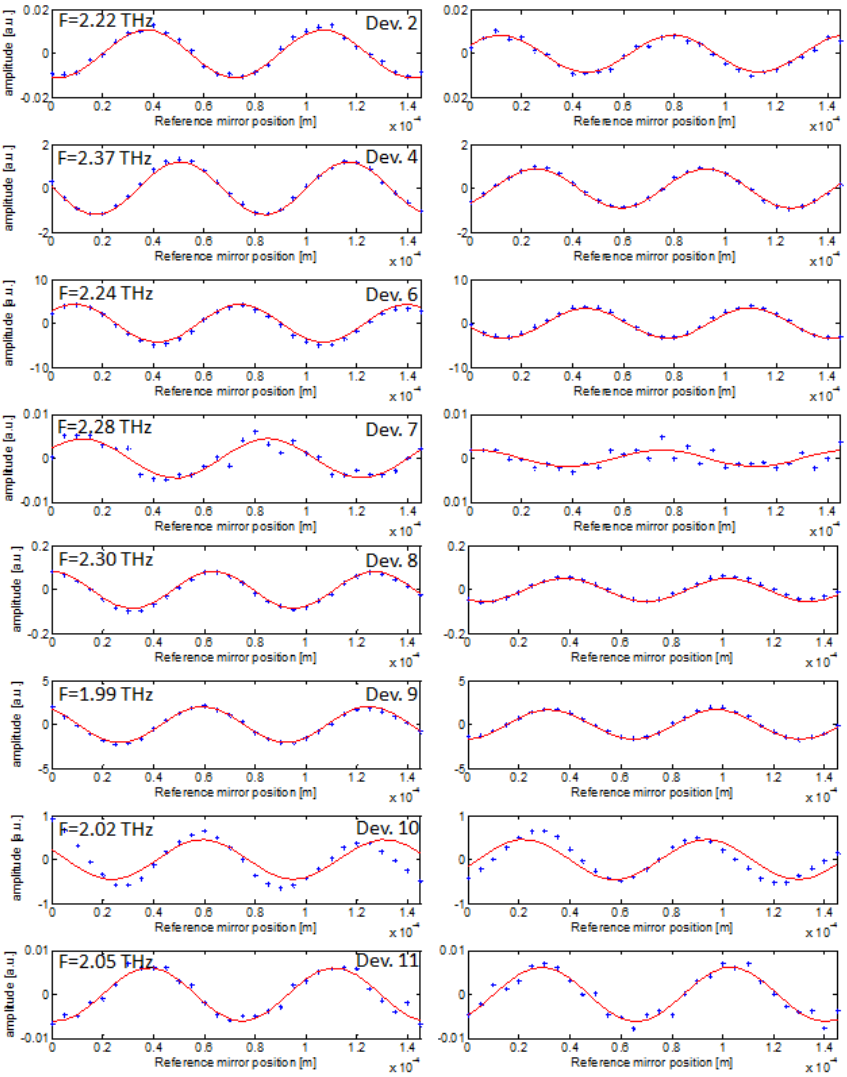

Figure 8. Interference signals (blue '+') and numerical fit (red solid trace) for various devices obtained as a function of position of the reference mirror. The first column shows signals when no sample is present. The second column shows interference signals when a 380-μm thick sample of polypropylene is inserted in the sample arm.

The interference patterns show clear sinusoidal modulation with mirror position for both the case without a sample (left column), and with a 380-μm thick sample (right column). Due to the long coherence length of QCL, the sinusoidal modulations are apparent even at large path differences between the reference and sample arms. This eliminates the need of finding the zero-path delay required in the time-domain approaches, further simplifying the interferometer setup. In order to resolve the air/polypropylene and polypropylene/metal interfaces, the algorithm shown in Figure 9 is used.

After the interference signal is acquired ('+' symbols in Figure 8) a numerical fit is used to determine the amplitude, period and phase of the modulation for each device (red trace in Figure 8). Amplitude normalization is performed, and the interference signals are summed, resulting in the traces shown in Figure 10. The first column of part a shows the case where no sample is present and all modulation frequencies add together when the path length difference between the interferometer arms is zero. Due to the limited number of QCLs, and the limited bandwidth (~300 GHz), side lobes appear between 0.5 to 1 mm and -1 to -0.5 mm. Phase and amplitude modulations resulting from the insertion of the sample result in the pattern shown in the second column. To resolve the interfaces, it is useful to measure the envelope

of the summation. In Figure 10 (a), right column, the air/polypropylene and polypropylene/metal interfaces become apparent.

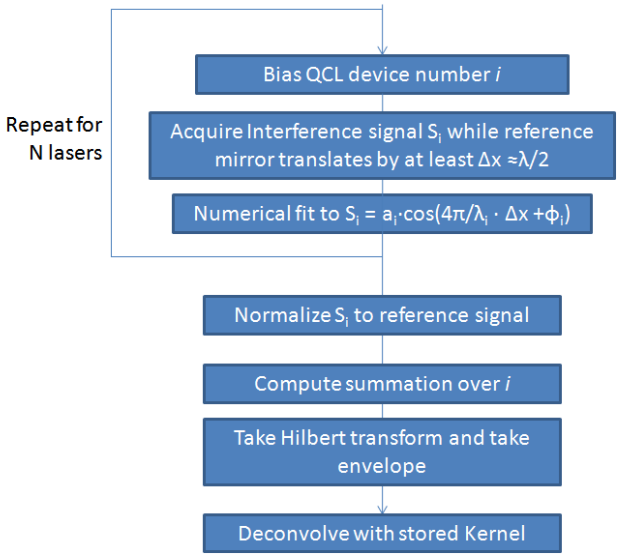

Figure 9. Algorithm for depth measurement of a sample.

The measured interfaces can be sharpened somewhat by de-convolving the measured signal (Figure 10(b)), using the reference signal as the kernel. Using the iterative Richardson-Lucy algorithm for N=20 iterations, the interfaces are sharpened in the trace of part b. The position of the air/polypropylene interface occurs at 380 µm because the sample arm is shortened after inserting a sample. However the path to the polypropylene/metal interface is effectively lengthened by the higher index polypropylene: (n_{poly} -1) ×380 µm = 160µm, giving out n_{poly} = 1.42, (Figure 10(c)). Without the knowledge of the index of refraction, it would appear that the sample is 380 + 140= 520 µm thick. Additional characterizations of the thickness measurement were done on 180-µm thick glass slides (Figure 10(d)). Only the glass/air interface was resolvable due to the strong attenuation in the glass.

The acquisition time of this experiment was ~40 s, discounting the ~5 s required for the lock-in amplifier to reacquire a phase lock when a laser is switched. The primary limitation on the acquisition speed is the large number (30) of reference mirror scan steps used to determine the amplitude and phase of the interference signals of Figure 10(a). System scan speed can be greatly increased by scanning only a small number of positions. As in typical near-IR OCT systems, it is possible to fix the position of the reference mirror altogether, resulting in halving of the axial range of the scan, but greatly increased scan speed while simplifying the mechanics [12]. The large translation of the reference mirror was done in this work to allow amplitude normalization, without which the reconstruction of the interferogram of Figure 10(a) for the limited number of lasers would not have resulted in cancelation away from the zero path delay (e.g., larger side lobes). Additional speed increases can be obtained by improving the electronics to eliminate the lock-in amplifier.

The FWHM depth resolution (z) is given by the bandwidth of the source as shown in Eq (2). For the present system, this limits the depth resolution to approximately 360 µm in polypropylene (n=1.42) or 470 µm in air, which is close to the measured FWHM of 440 µm in Figure 10(a). A finer depth resolution can be achieved by further improving the frequency coverage.

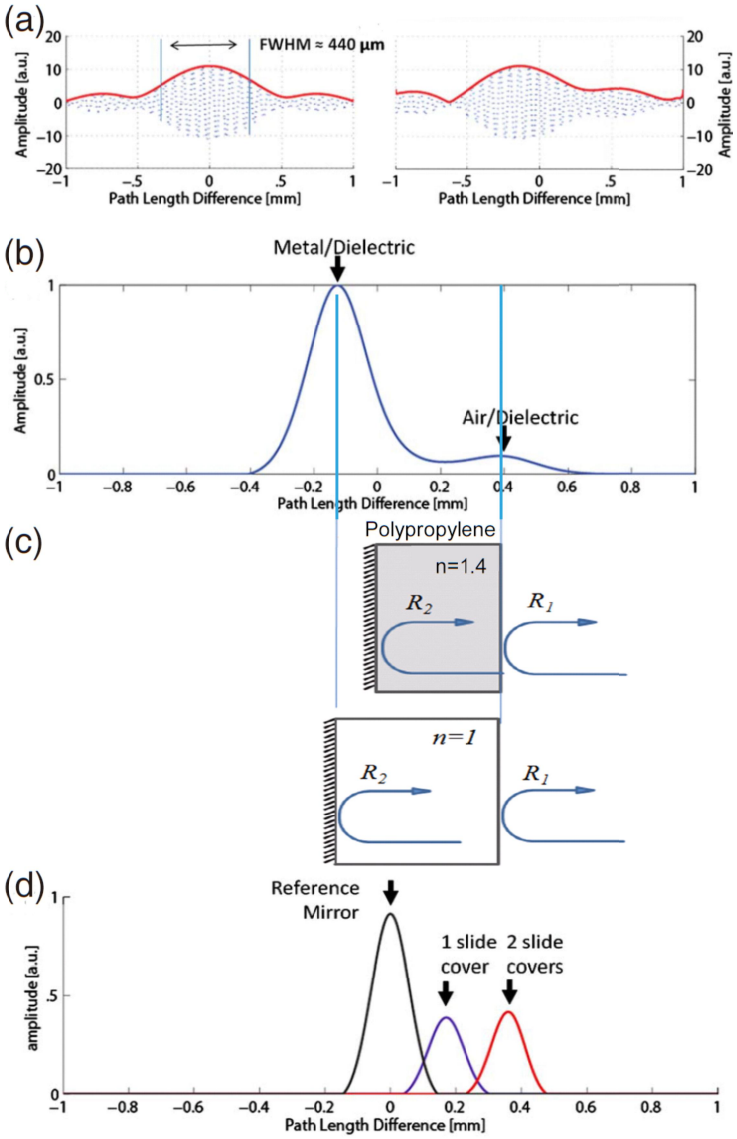

Figure 10. Part (a). Reconstructed interferogram (summation of normalized measured signals) as a function of path length difference between the interferometer arms. The left column shows results without a sample while the second column has a 380-µm thick polypropylene sample. The numerical fitting envelope function was shown in red. Part (b) shows the numerically sharpened version of right column in (part a) using deconvolution. The interfaces of the thin sample are clearly visible, demonstrating the key concept of SS-OCT: axial tomography. Part (c) shows the effect of inserting a polypropylene sample in path of the interferometer. Due to the index of polypropylene, the back mirror appears at ~ 160 µm further from the zero path difference point. The total thickness has the appearance of a 540-µm thick piece of n = 1 sample. Part (d) the reconstructed signals from one and two 180-µm thick glass samples.

5. RECENT IMPROVEMENT ON 3RD DFB THZ QCL DESIGN FOR WIDE FREQUENCY COVERAGE

One determining factor of spatial resolution in a THz SS-OCT system is the frequency coverage of swept source. In our initial implementation of DFB QCL array, a 320-GHz frequency coverage was obtained. In order to achieve larger frequency coverage, we improve upon the previous design by changing the shape of the corrugated gratings from a traditional square tooth to a tapered shape as shown in Figure 11(b). According to an electromagnetic finite-element

(FEM) simulation, the taper-horn shape increases the radiation loss from the unwanted upper band-edge mode while marginally reducing the radiation loss for the desired third-order DFB mode, hence improving mode selectivity and thus more robust single-mode operation. Effectively, this approach leverages a trade-off between the output power efficiency and mode discrimination. With this improved frequency selectivity, we realize a linear frequency coverage of **440 GHz**, from 4.61 to 5.05 THz (from a different gain medium used in the previous QCL array) as shown in Figure 11(a), which covers ~ 80% of the gain spectrum. The linearity of the DFB QCL arrays was also improved (see the inset for near uniform frequency spacing between adjacent elements).

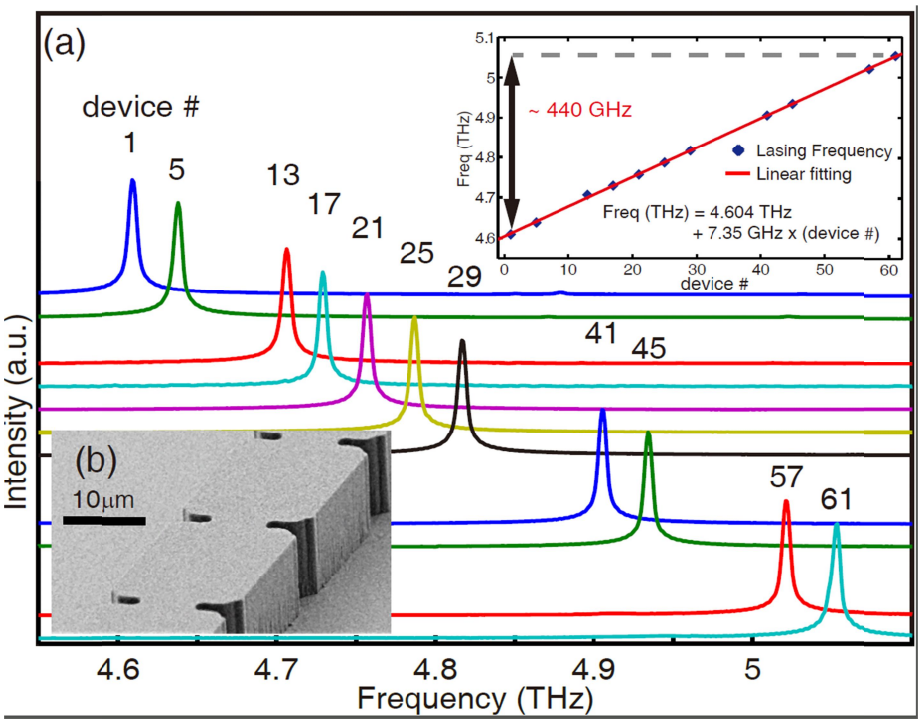

Figure 11. (a) Spectra of an array with 11 devices operating in pulsed mode (at 10 K) demonstrating the frequency selectivity of a third-order DFB QCL array. (b) Scanning electron microscope (SEM) image for a taper-horn third-order DFB laser.

6. CONCLUSION

In summary, we have demonstrated the tomography of a dielectric sample using a frequency agile QCL array source at terahertz frequencies. The electrically switched source suggests fast axial scan speeds. Improved axial resolution will result from a spectrally broader source. An increase in the number of elements in the source will allow greater scan depth and potentially a fixed reference mirror interferometer, greatly enhancing the scan speed and simplicity of the system. We also addressed the issue of limited frequency bandwidth of our first DFB QCL array by introducing new type of DFB structure for better mode selectivity. A ~30% improvement in frequency coverage is achieved (from 320 to 440 GHz).

This work is supported by the NASA/Kennedy Space Center under contract NNX11CC66C and the NSF. This work was performed, in part, at CINT, a U.S. DOE Office of Basic Energy Sciences user facility. Sandia National Laboratories is a multiprogram laboratory managed and operated by Sandia Corporation, a wholly owned subsidiary of Lockheed Martin Corporation, for the U.S. Department of Energy's National Nuclear Security Administration under contract DE-AC04-94AL85000.

REFERENCES

[1] Mittleman D. M., Hunsche S., Boivin L., and Nuss M. C., "T-ray tomography," Opt. Lett. 22, 904 (1997).

[2] Zhong S., Shen Y. C., Ho L., May R. K., Zeitler J. A., Evans M., Taday P. F., Pepper M., Rades T., and Gordon K. C., "Non-destructive quantification of pharmaceutical tablet coatings using terahertz pulsed imaging and optical coherence tomography, " Opt. Lasers Eng. 49, 361 (2011).

[3] Yasui T., Yasuda T., Sawanaka K., and Araki T., "Terahertz paint meter for noncontact monitoring of thickness and drying progress in paint film," Appl. Opt. 44, 6849-6856 (2005).

[4] Bennett D. B., Taylor Z. D., Tewari P., et al, "Terahertz sensing in corneal tissues," J. Biomed. Opt., 16(5), 057003 (2011).

[5] Crawley D., Longbottom C., Wallace V.P., Cole B., Arnone D., Pepper M., "Three-dimensional terahertz pulse imaging of dental tissue," J. Biomed. Opt., 8(2), 303-7 (2003).

[6] Fercher A. F., Hitzenberger C. K., Kamp G., and El-Zaiat S. Y., "Measurement of intraocular distances by backscattering spectral interferometry," Opt. Commun. 117, 43 (1995).

[7] Chinn S., Swanson E., and Fujimoto J., "Optical coherence tomography using a frequency-tunable optical source," Opt. Lett. 22, 340-342 (1997).

[8] Williams B. S., Kumar S., Hu Q., and Reno J. L., "Distributed-feedback terahertz quantum-cascade lasers with laterally corrugated metal waveguides," Optics Letters 30, 2909 - 2911 (2005).

[9] Amanti M. I., Fischer M., Scalari G., Beck M., and Faist J., "Low-divergence single-mode terahertz quantum cascade laser," Nat Photon 3, 586-590 (2009)

[10] The gain threshold is a measure of the gain required to support lasing, which occurs when gain=loss. Therefore all losses should be included. Additional loss mechanisms not specifically included in these plots are free carrier losses, and intersubband absorption losses

[11] Kumar S., "Development of Terahertz Quantum-Cascade Lasers," Massachusetts Institute of Technology, (2007).

[12] Choma M., Saruni M. c, Yang C., and Izatt J., "Sensitivity advantage of swept source and Fourier domain optical coherence tomography," Opt. Express 11, 2183-2189 (2003).